Transp Porous Med (2011) 90:363–391
DOI 10.1007/s11242-011-9789-7

Effect of Network Structure on Characterization and Flow Modeling Using X-ray Micro-Tomography Images of Granular and Fibrous Porous Media

Pradeep Bhattad · Clinton S. Willson · Karsten E. Thompson

Received: 21 May 2010 / Accepted: 1 June 2011 / Published online: 22 June 2011

Abstract Image-based network modeling has become a powerful tool for modeling transport in real materials that have been imaged using X-ray computed micro-tomography (XCT) or other three-dimensional imaging techniques. Network generation is an essential part of image-based network modeling, but little quantitative work has been done to understand the influence of different network structures on modeling. We use XCT images of three different porous materials (disordered packings of spheres, sand, and cylinders) to create a series of four networks for each material. Despite originating from the same data, the networks can be made to vary over two orders of magnitude in pore density, which in turn affects network properties such as pore-size distribution and pore connectivity. Despite the orders-of-magnitude difference in pore density, single-phase permeability predictions remain remarkably consistent for a given material, even for the simplest throat conductance formulas. Detailed explanations for this beneficial attribute are given in the article; in general, it is a consequence of using physically representative network models. The capillary pressure curve generated from quasi-static drainage is more sensitive to network structure than permeability. However, using the capillary pressure curve to extract pore-size distributions gives reasonably consistent results even though the networks vary significantly. These results provide encouraging evidence that robust network modeling algorithms are not overly sensitive to the specific structure of the underlying physically representative network, which is important given the variety image-based network-generation strategies that have been developed in recent years.

P. Bhattad · K. E. Thompson (✉)
Department of Chemical Engineering, Louisiana State University, Baton Rouge, LA 70803, USA
e-mail: karsten@lsu.edu

P. Bhattad
e-mail: pradeep@lsu.edu

C. S. Willson
Department of Civil and Environmental Engineering, Louisiana State University, Baton Rouge,
LA 70803, USA
e-mail: cwillson@lsu.edu

Keywords Pore network generation · Pore network modeling · Permeability · Pore structure characterization · 3D image processing · X-ray micro-tomography

1 Introduction

Flow in porous media occurs in engineering applications such as oil recovery, flow in packed bed reactors, membrane separations, and subsurface solute transport. While Darcy's law or similar approaches can be used for modeling flow at the continuum scale, the accuracy of such simulations requires correct estimation of one or more parameters such as porosity, heterogeneity, relative permeability, capillary pressure relationships, etc. These parameters are typically measured experimentally. However, microscale simulations are becoming increasingly viable methods for obtaining this information. The most fundamental approach is direct solution of the equations of motion in the pore space using an approach such as the finite element, finite volume, or lattice Boltzmann method. If performed on a sufficiently large domain, then information such as fluid flowrates, pressure gradients, or solute distributions can be used to determine relevant macroscopic parameters. The large computational cost associated with these methods can reduce the effectiveness of these techniques because of time and/or size limitations.

Network modeling is an alternative technique for pore-scale flow modeling, which is less rigorous than the aforementioned methods but is dramatically more efficient computationally. In network modeling, the pore space is discretized into pores and connecting pore throats. A mass balance is imposed at each pore, and flow through the pore throats is approximated by one-dimensional Poiseuille-type equations. The consequence of this coarsening of the pore space is that sub-pore phenomena cannot be simulated directly; however, network modeling allows flow to be modeled over orders-of-magnitude larger physical domains. Network model simulations have been used to study processes such as imbibition (Fenwick and Blunt 1998; Gladkikh and Bryant 2005), drainage (Blunt et al. 1992; Fenwick and Blunt 1998), single phase and relative permeability computation (Bryant and Blunt 1992; Oren and Bakke 2002), the effects of pore structure on relative permeability (Bryant and Johnson 2003; Al-Kharusi and Blunt 2008), capillary pressure behavior (Fatt 1956; Silin and Patzek 2006; Al-Kharusi and Blunt 2008), residence time distributions (Thompson and Fogler 1997), dispersion (Sahimi et al. 1986), measurement of interfacial area and fluid phase distribution (Dalla et al. 2002), relationships between non-wetting phase distributions and pore geometry (Hilpert et al. 2000), non-Newtonian flow in packed beds (Balhoff and Thompson 2004), and with continuum models in a multiscale framework (Balhoff et al. 2007, 2008).

The predictive capability of network models depends on the process being modeled, the assumptions made in approximating the fluid mechanics, and how well the network structure depicts the actual geometry and topology of the real porous media. With the widespread use of non-destructive 3D imaging and the development of image-based modeling techniques, there is increased interest in using network models in a predictive sense (in contrast to studies which aim to uncover qualitative phenomenological behavior).

One of the difficulties in image-based network modeling is the ambiguity in the physical or geometric definition of what is termed a pore or pore throat in various types of materials. This ambiguity prevents the development of a universal definition of network structure. Consequently, multiple network structures can be created for the same material or 3D data set and there exists no straightforward way to define whether one network is more correct than another (without validation from a rigorous sub-pore-scale model).

In this article, we examine a range of networks that, while created from the same porous media, exhibit significantly different geometric structures. We quantify the impact of these differences on selected simulations. Three materials are used: a random packing of spheres, a random packing of non-spherical grains, and a random packing of cylinders. All three materials were imaged using XCT, thus providing detailed 3D structural data. Image-based network models were created using in-house algorithms, and the differences in network structure, single-phase flow, and quasistatic displacement were studied in an effort to quantify the impact of variations in network structure.

2 Background

2.1 Network Modeling

The earliest network models are attributed to Fatt (1956) and consisted of highly simplified two-dimensional networks of tubes arranged on square or hexagonal lattices. The networks had fixed coordination number and the pores were located at the intersection of the tubes but were considered to have no volume. Experimentally obtained pore-size distributions were imposed onto the networks by randomly assigning the tube size distribution. Later, Chatzis and Dullien (1977) reported that three-dimensional networks of tubes differ substantially from 2D networks for immiscible displacement and the breakthrough condition for multiphase flow depends on the interconnectivity and dimensionality of the network. Similar models have since been used to simulate two- and three-phase imbibition and drainage (Blunt et al. 1992, 1994; Fenwick and Blunt 1998). To create more realistic networks, connectivity is often varied by randomly removing bonds from the underlying lattice structure. Pore-size distributions can be assigned based on experimental porosimetery results (e.g., Wardlaw et al. 1987, who decorated networks using pore and pore–throat size correlations measured from Berea sandstone).

A second generation of network models was developed beginning with Bryant et al. (1993); Bryant and Johnson (2003) in which the network is mapped directly from the void structure in a three-dimensional packing instead of creating a statistically equivalent network on a lattice structure. This approach can be used with actual materials if the detailed particle structure is available (Bryant et al. 1993) or on computer-generated materials (Thompson and Fogler 1997; Al-Raoush et al. 2003; Hilpert et al. 2003). The advantage of physically representative networks is that pore-scale spatial correlations are incorporated into the network. Additionally, because the network is a direct mapping of a well-defined 3D structure, it reduces the ability to incorporate adjustable parameters into the model.

Recently, a third-generation approach has evolved in which networks are mapped directly from high-resolution digital images of porous media. Early work in this area includes Thovert et al. (1993), Lindquist et al. (1996), and Delerue et al. (1999). This approach has since become widely adopted because it has the same advantages described in the previous paragraph (incorporation of spatial correlations, elimination of adjustable parameters) but can be applied to essentially any type of porous media rather than only simple structures such as sphere packings. The digital data can be obtained from either computer-generated or real structures. The former approach represents a unique tool for material design; the latter approach, termed image-based network modeling, offers obvious appeal because of the opportunity to study real materials. 3D images of real porous media can be obtained using serial sectioning (Adler et al. 1990; Lymberopoulos and Payatakes 1992; Vogel and Roth 2001; Silin and Patzek 2006; Jiang et al. 2007), which can give very high resolution in the plane of the slices but is destructive and less amenable to automation. Hence, the more popular approaches are non-destructive imaging techniques such as XCT (Petrovic et al. 1982; Auzerais et al. 1996; Al-Raoush and Willson 2005a,b; Ruffino et al. 2005; Neethirajan and Jayas 2008), MRI (Baldwin et al. 1996; Botto et al. 1996; Kose 1996; Pauli et al. 1997), and confocal microscopy (Mickel et al. 2008). Resolution in these techniques typically ranges between 0.1 and 100 μm, and the final data sets provide quantitative descriptions of the 3D pore structure.

2.2 Image-Based Network Generation

Transforming the voxel description of the void space into a network is a challenge for a number of reasons. In the original data, the void space is often described by upwards of one billion voxels on a regular grid, whereas the network is an unstructured grid with orders of magnitude fewer discrete elements. Additionally, this transformation from voxels to a pore network must be performed in a way that retains the essential features of the pore structure, despite the fact that no definitive rules have been established for how to discretize the continuum void space into a series of pores and pore–throats.

The various algorithms proposed in literature for extracting pore networks from 3D images fall into two broad categories: skeletonization algorithms and geometric algorithms. Skeletonization algorithms typically employ a voxel-scale approximation of the medial axis to create a graph of the pore space. Pores are placed at the nodal junctions of the skeleton and pore–throats are defined by the curved elements of the skeleton that connect these nodes. The skeleton is decorated with network parameters, such as pore sizes, which define the pore morphology. This approach has been used to simulate numerous processes and properties in rock samples (Spanne et al. 1994; Bekri et al. 2000; Prodanovic et al. 2007; Gaviglio et al. 2009). Alternatives to the medial axis include geometrical thinning or hybrids of the two techniques (Saito and Toriwaki 1994; Pudney 1996, 1998; Jiang et al. 2007; Prodanovic et al. 2007).

The other major approach to network generation uses some type of geometric analysis to define pore locations, and then builds the network structure from this information. Prior to the development of voxel-based techniques, the Delaunay tessellation (Bryant et al. 1993; Thompson and Fogler 1997) or a modified Delaunay tessellation (Al-Raoush and Willson 2005a,b) was used to define both pores and network interconnectivity. Delaunay-based techniques have been used to study packed beds and natural porous media, including phenomena such as dynamic and quasi-static imbibition (Gladkikh and Bryant 2003, 2005, 2007), interfacial area (Gladkikh and Bryant 2003), drainage (Thompson and Fogler 1997), and relative permeability (Bryant and Blunt 1992). Al-Raoush et al. (2003) compared pore structural properties of networks using medial-axis-based transforms versus modified Delaunay tessellation schemes on computer-generated regular and random packing of spheres. Silin and Patzek (2006) proposed a voxel-based maximum-inscribed sphere approach to map pore network structures. Thompson et al. (2008) developed a Delaunay-based method that can be used with voxel data if the locations of particles in a packing are known. Al-Kharusi and Blunt (2007, 2008) have used the maximal inscribed sphere technique developed by Silin and Patzek (2006) to generate networks from tomography images of sandstone and other natural rocks, and modeled two- and three-phase relative permeability and capillary pressure curves.

One of the problems in network generation and network modeling is the lack of a specific definition for what constitutes pores and pore throats in real materials with complicated pore geometries. A second problem is understanding how differences in this definition of a pore can effect discretization and network topology. A third problem is that many questions remain unresolved regarding whether uniqueness can be expected from a network model (for a specific CT data set for instance) and/or whether non-uniqueness has a detrimental effect on numerical simulation. For example, Vogel (2000) was able to create different lattice-based topologies that nonetheless produced similar water retention curves. In contrast, Anrs et al. (2004; Mahmud 2007) demonstrate that network topology (including random vs. spatially correlated networks) does affect relative permeability.

This study focuses largely on the second and third issues described above, through examination of significantly different network structures that were created from the same porous media images. It is worth emphasizing that the goal is not to compare skeletonization versus geometric techniques (all networks discussed below are created using geometric-based algorithms). Similarly, the goal is not to assess the accuracy of physical transport properties obtained from the network simulations. Instead, the objective is to understand the sensitivity of numerical simulation to differences in network topology in a situation where all the networks are created using viable image-based network generation techniques.

2.3 Grain-Based Algorithm

The grain-based approach for network generation is a two-step process: 1. computationally reconstruct particles from the XCT image; 2. use the particulate structure as a template to create the pore and pore–throat network. The rationale for this approach is that pores are formed by clusters of grains or particles in an unconsolidated granular material. Hence, using particles as a template ensures that the correct characteristic scale is used to define the pore structure.

The grain reconstruction step transforms a binary image (e.g., solid-phase voxels equal 1; void-phase voxels equal 0) into a grain-scale map in which each solid-phase voxel is tagged with the grain number to which it belongs. Grain identification is a non-trivial procedure for most any material except idealized sphere packings. The algorithm uses a combination of erosion followed by non-linear optimization to search for the maximal inscribed sphere that is contained inside each grain. Once the grain centers are located (which correspond to the locations of the maximal inscribed spheres, not the centers of mass of the grains), voxels belonging to that particular grain are collected from the center moving outward using a variant of the watershed algorithm. Details can be found in Thompson et al. (2006). Once every solid-phase voxel is tagged with its respective particle number, any particle or grain in the packing can be reconstructed from the digital image simply by retrieving the corresponding cluster of voxels. This approach allows a number of physical properties of the material to be computed, including total particle surface areas, fraction of surface areas exposed to the void phase, number of grain–grain contacts and the surface area of these contacts (limited by voxel resolution), grain volumes, grain orientations, grain locations, and grain aspect ratios.

The second step in the grain-based network-generation process is to create the pore and pore–throat map of the void space using the granular structure of the material as a template. For sphere packings and other materials made from compact grains, clusters of four or more particles create pores in the void structure. The particle cluster that forms a pore also has smaller gaps that lead into and out of the central pore (which are pore throats). Hence, using the granular structure as a template for the network structure is a more physically appealing approach than working directly from the voxel map itself. Mellor (1989), Bryant et al. (1993), and Thompson and Fogler (1997) have used the Delaunay tessellation as a mathematical tool for transforming the continuous, interconnected void space in a sphere packing into a discrete set of pores and pore–throats. This approach was modified by Al-Raoush et al. (2003) to allow more flexibility in the network structure, including variable pore coordination numbers (as opposed to the fixed value of four that is dictated by the

Delaunay tessellation). In the current approach, the modified Delaunay tessellation (MDT) approach is used in an implementation that operates on voxel images. In summary, it is comprised four steps:

1. The Delaunay tessellation (operating on the granular structure in the material) is used to locate possible locations of pores.
2. The pore locations are confirmed and refined using a non-linear optimization procedure that locates maximal inscribed spheres in the void space.
3. Voxels belonging to a given pore are collected by moving from the center outward using a watershed-type algorithm.
4. The pore-network structure is created from the tagged voxels in the pore space.

Parameters that describe the pore network include inscribed pore radii, pore volumes, throat radii, throat cross-sectional areas, throat surface areas, throat wetted perimeters, throat hydraulic conductances, and of course the connectivity of the network itself. More details about how the grain-based network generation algorithm is applied to real materials can be found in Thompson et al. (2008).

2.4 Voxel-Based Algorithm

The algorithm described in the previous section can be applied to unconsolidated granular or particulate materials. However, it is not designed to operate on many other types of materials including fibrous materials, carbonates, highly consolidated materials, or solid foams. In these situations, the only viable approaches at present are voxel-based network generation techniques.

In this study, we use an algorithm that creates a pore-network mapping of the void space directly from a binary (phase segmented) voxel image. Because the grain identification and Delaunay tessellation process cannot be used as a template, the main difference in the voxel-based algorithm is identification of pores. Once the set of maximal inscribed spheres is found, the network generation process is completed in the same way as it is with the grain-based algorithm.

As with the grain-based algorithm, each pore is characterized by a maximal inscribed sphere (i.e., a hypothetical sphere that is constrained from both movement and growth by its contact with surrounding solid phase). In all cases, we find the maximal inscribed spheres using the same non-linear optimization process used with the grain-based algorithm. However, because this optimization procedure is computationally expensive, we have devised a number of different schemes to define subsets of seed voxels from which to run the optimization. In this study, we employ three approaches:

1. Perform a voxel burn (Thovert et al. 1993; Lindquist et al. 1996; Lindquist and Venkatarangan 1999) to find approximate local maxima in the distance function from the surface; use these locations as seeds for potential pore centers.
2. Use all void-phase voxels as potential seeds for the non-linear optimization, but eliminate all voxels that are contained inside a maximal inscribed sphere once is it found.
3. Use all void-phase voxels as seeds for the non-linear optimization.

(Rationale for these approaches and additional details are given below in Sects. 3.3–3.5.) Unfortunately, there is no easy way to determine whether one approach is more correct than another. For a sphere packing, there exists a finite number of maximal inscribed spheres, which can all be located by a simple search procedure. However, for non-spherical particles, this set can increase significantly. Furthermore, when particles are described by a voxel

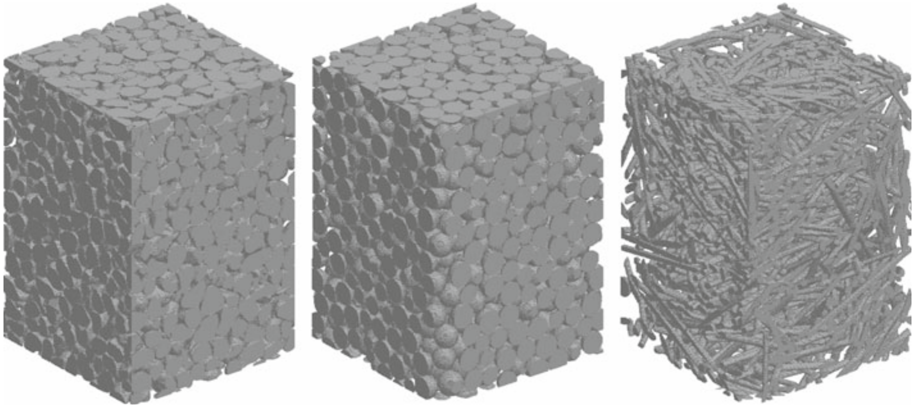

Fig. 1 Segmented image of packings. *Left* to *right*: sand, spheres, and cylinders. Image size = $350 \times 350 \times 520$. Resolution = 6.603µm/voxel side

image, the particle surfaces are not defined exactly, which can compromise the accuracy of the processes. In general, the number of maximal inscribed spheres (and their locations) that are fed to the network generation algorithm are determined by the method used to locate them and how aggressive the merging process is for overlapping spheres.

Once the set of maximal inscribed spheres is found (and any merging procedures are applied), the network is constructed in the same manner as with the grain-based algorithm (see steps 3 and 4 in the procedure outlined in the previous section).

3 Materials and Methods

Three types of packing materials were chosen to create the porous media: (i) smooth soda-lime glass spheres (250–297 µm , Mo-sci specialty products LLC); (ii) sand particles of similar size as the spheres but with more irregular grain shapes (210–297 µm, Accusand, Unimin corporation); (iii) cylinders that were packed randomly to create a simulated high-porosity fibrous material (diameter 90–100 µm and aspect ratio 10–20, Mo-sci specialty products LLC). The random packings were created by adding the packing media into plastic columns, and then shaking the columns using a vortex mixer to help remove macroscopic heterogeneity (the goal being to obtain microscopically heterogeneous but macroscopically uniform packings). The columns were imaged using synchrotron XCT to obtain three-dimensional gray-scale images (energy 35 keV and resolution 6.603µm/voxel; see acknowledgements for imaging facilities). Internal sections of the 3D images of size $350 \times 350 \times 520$ were selected from the centers of the columns to avoid wall effects. A combination of anisotropic diffusion and indicator kriging was used for image segmentation (Bhattad et al. 2010). A non-linear anisotropic diffusion algorithm was used for image de-noising (Frangakis and Hegerl 2001; Weickert and Scharr 2002; Scharr and Spies 2005) and the modified gray-scale images were segmented using an indicator-kriging thresholding algorithm similar to Oh and Lindquist (1999) to obtain binary images containing void and solid phases. The phase-segmented data are shown in Fig. 1. From each segmented image, four networks were created. Network properties were computed after cropping a length of one particle diameter from all sides of a network structure to avoid including information associated with partial pores at the network surfaces.

Table 1 Parameters used in the generation of four networks

	GB1	VB1	VB2	VB3
Algorithm				
Grain-based	X			
Voxel-based		X	X	X
Pore Search Method				
Tessellation of grains	X			
Burn maxima		X		
Subset void voxels			X	
All void voxels				X
Burn coordination number				
6		X		
Merge criteria				
None				X
Center contained	X	X	X	
Throat connections				
All connections	X	X	X	X

3.1 Pore Networks

Four networks were generated from each of the XCT images (spheres, sand, and cylinders). One network from each XCT image was generated using the grain-based approach. The other three were created using the more general voxel-based approach, which is not limited to granular materials. The differences between the latter three networks is the methodology used to locate pores. Varying the pore search technique causes more than two orders of magnitude variation in the number of pores, which in turn leads to differences in other network parameters. Specific parameters used in the network-generation process are given in Table 1. Thin cross sections of four different networks (from the sphere pack) are shown in Fig. 2 using stick-and-ball depictions.

Due to excessive computation times for the VB2 and VB3 networks in the high-porosity cylinder packs, the cylinder data were cropped to $150 \times 150 \times 150$ size and all four networks were generated from the smaller image for consistency in comparison. The smaller networks were tested against the larger networks for GB1 and VB1, and these tests indicate the 150^3 data were sufficient to generate representative volumes (see the appendix).

3.2 Network GB1

For the two particulate materials, the grain-based approach is expected to create a physically representative network with the appropriate characteristic scales because the network is built using the granular structure as a template. For the cylinders, there is no physical basis for using this algorithm, but it is used nonetheless for the purpose of comparison. (It should be noted that while the grain reconstruction and tessellation process are used to define seeds for locating pores, the final pore locations are defined using the XCT data. Hence, even with the cylinder packing, the network pores are indeed maximal inscribed spheres in the image.) For all three materials, pairs of pores are merged if the center of one pore is contained inside a neighboring pore.

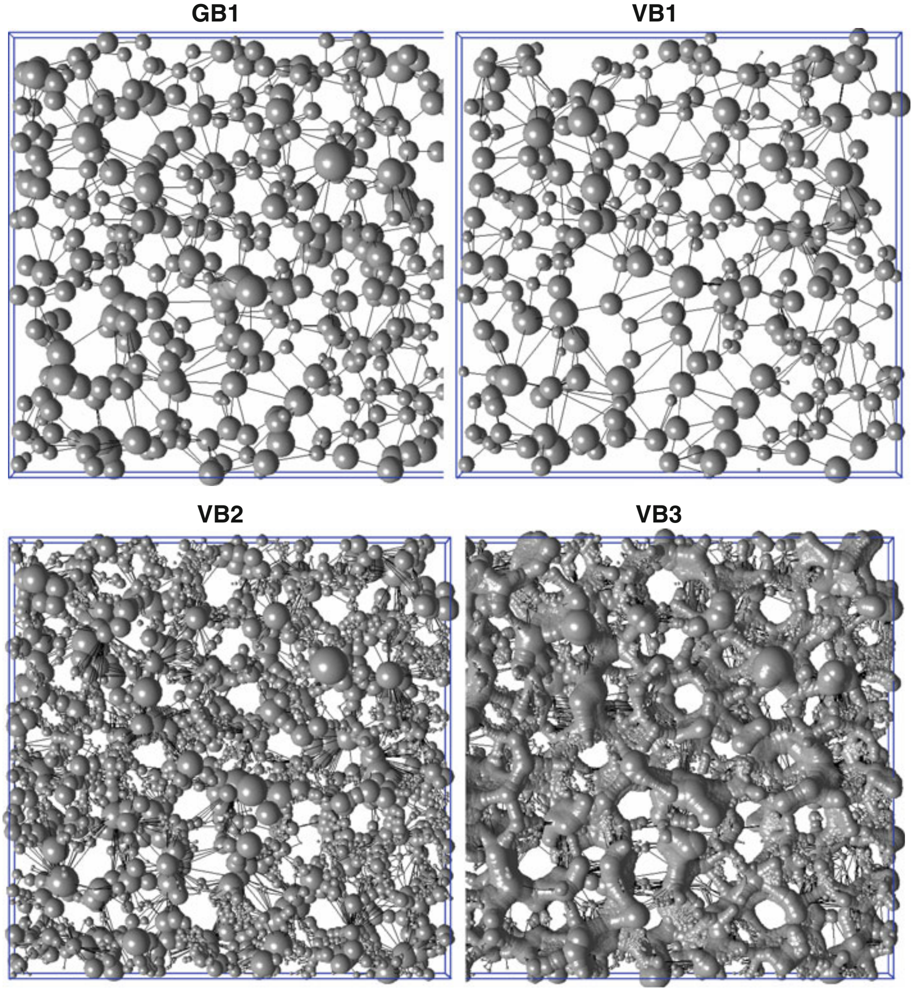

Fig. 2 Ball-and-stick representation of section of pore networks generated using the sphere-pack data

3.3 Network VB1

All three VB networks are created using the voxel-based approach. For network VB1, pore seeds are identified from the local maxima in the void-phase-burn number, and the non-linear optimization algorithm refines these initial seeds so that pores correspond to maximal inscribed spheres. Pairs of pores are merged if the center of one pore is contained inside a neighboring pore. Because the burn maxima is a somewhat "quick and dirty" method for locating potential pores, this algorithm runs quickly and it results in the fewest number of pores of any of the networks studied here. Because the algorithm does not rely on discretization of the solid phase into individual grains, it is appropriate for both the particulate and the fibrous materials.

3.4 Network VB2

For the VB2 network, every void-phase voxel is a potential seed for the non-linear optimization procedure that locates maximal inscribed spheres. However, to save computation time, each time a maximal sphere is located, the voxels inside this sphere are removed from the list of possible seeds (the rationale being that most of these voxels would lead to the same maximal inscribed sphere, thus creating redundancy in the search). This strategy creates a medium-density network. It is slower than the VB1 approach, but dramatically faster than using every void-phase voxel as a potential seed. As with the previous two approaches, pairs of pores are merged if the center of one pore is contained inside a neighbor.

3.5 Network VB3

To create the VB3 network, every void-phase voxel is used as a seed to locate maximal inscribed spheres. Additionally, every unique maximal inscribed sphere (pore) is retained, regardless of the degree of overlap with a neighboring pore. This strategy produces the maximum number of pores of any combination of parameters in our set of algorithms, which typically results in overlapping spheres that form caterpillar-like structures that wind through the pore space (see Fig. 2d). This network generation process is very slow. It should also be noted that the large number of unique maximal inscribed spheres are due in part to the approximate distance functions that must be used in a voxelized structure, combined with the staircase-like surfaces that are found in any voxel-based data set.

4 Results and Discussion

The networks were analyzed using three different comparisons: physical structure, single-phase flow (permeability), and quasi-static drainage (which generates the primary drainage branch of a capillary pressure curve).

4.1 Network Structure

Figures 2 and 3 are ball-and-stick representations of thin sections of selected networks, which provide qualitative insight into the different structures. The balls in the images are the maximal inscribed spheres associated with each pore. The sticks simply denote pore–throat connections between pores; no attempt is made to denote pore–throat diameter in these illustrations. The images shown are thin sections of the 3D networks, which allows easier visualization of the network structure. Average network properties are given in Table 2 and are discussed below.

4.1.1 Pore Density

As shown in Fig. 2 and Table 2, varying parameters in the network-generation algorithms results in pore densities (number of pores per unit volume) that span more than two orders of magnitude. Because no definitive rules exist for discretization of a network into pores and pore throats, choosing whether one network generation scheme is more appropriate than another is largely speculative (at least until the modeling community begins to accumulate additional data about these effects). Furthermore, the decision about which network is best will likely depend on the situation. For instance, if the network model is to be used for

Table 2 Physical properties of pore networks generated from the sphere, sand, and cylinder data

	Sphere				Sand				Cylinder			
	GB1	VB1	VB2	VB3	GB1	VB1	VB2	VB3	GB1	VB1	VB2	VB3
Domain volume before cropping	1.83E10	1.83E10	1.83E10	1.83E10	1.83E10	1.83E10	1.83E10	1.83E10	9.72E08	9.72E08	9.72E08	9.72E08
Domain volume before cropping	1.03E10	1.03E10	1.03E10	1.03E10	1.03E10	1.03E10	1.03E10	1.03E10	9.72E08	9.72E08	9.72E08	9.72E08
Porosity before cropping	35.50	35.50	35.50	35.50	31.04	31.04	31.04	31.04	70.54	70.54	70.54	70.54
Porosity after cropping	34.76	34.67	34.85	34.76	30.40	30.55	30.47	30.56	70.54	70.54	70.54	70.54
Number of particles	654	–	–	–	691	–	–	–	402	–	–	–
Particle radii (µm)	125.00	–	–	–	105.00	–	–	–	45.00	–	–	–
Number of pores	3243	2363	35403	262665	4494	3796	63417	319500	908	298	2704	34208
Avg. pore volume	1.11E06	1.52E06	1.02E05	1.37E04	6.99E05	8.31E05	4.96E04	9.88E03	4.07E09	2.30E06	2.54E05	2.00E04
Coordination number	5.95	5.98	5.34	9.00	5.87	6.08	5.49	8.39	6.72	7.45	6.03	10.02
Inscribed pore radii (µm)	41.77	39.92	16.63	29.82	30.72	28.74	13.60	22.82	40.74	53.60	26.03	44.41
Inscribed throat radii (µm)	27.12	25.90	14.80	26.46	20.41	18.73	12.59	20.88	27.71	31.89	21.01	38.39
Dimensionless inscribed pore radii	0.33	0.32	0.13	0.24	0.29	0.27	0.13	0.22	0.91	1.19	0.58	0.99
Dimensionless inscribed throat radii	0.22	0.21	0.12	0.21	0.19	0.18	0.12	0.20	0.62	0.71	0.47	0.85
Pore/throat aspect ratio	1.54	1.54	1.12	1.13	1.51	1.53	1.08	1.09	1.47	1.68	1.24	1.16

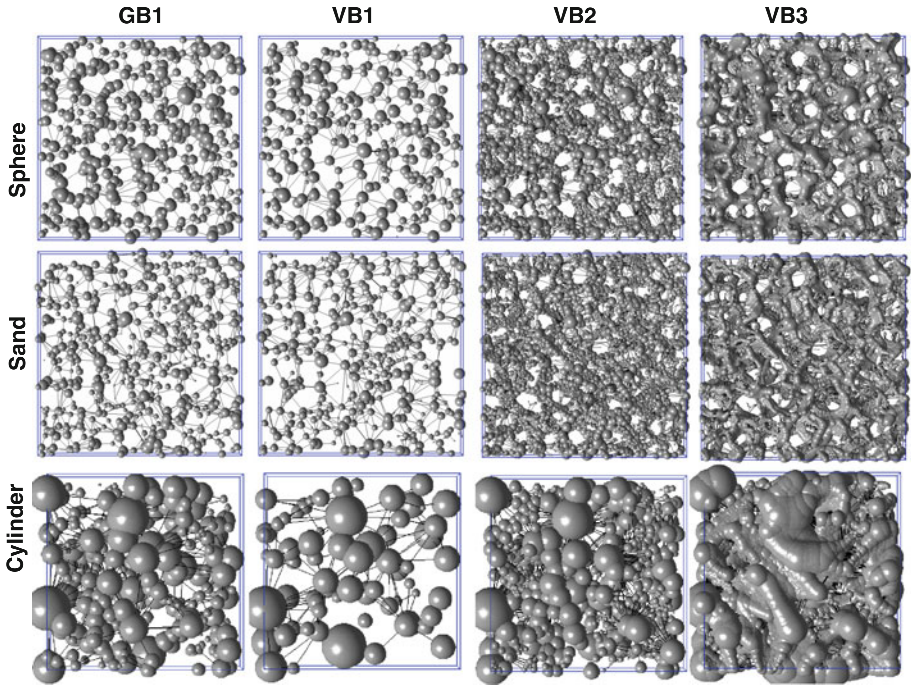

Fig. 3 Ball-and-stick representation of section of pore networks

characterization (pore-size distribution, pore coordination number, etc.), one might argue that the high-pore-density structure shown in Fig. 2d is not consistent with our typical view of pores and pore–throats. However, if the network is viewed as nothing more than a numerical discretization scheme for flow modeling, then the best network should be the one that provides the best accuracy, irrespective of whether it has representative pore-size distributions or coordination numbers. Finally, it should be emphasized that the ability to define strict discretization rules depends largely on the type of data describing the porous medium. For example, computer-generated packings of spheres and cylinders give exact description of the void space, and each of these packings has a finite number of maximal inscribed spheres (Zhang 2006). This fact might be used to place an upper bound on pore density. However, voxel-based data introduces error into the description of the void-space geometry, which gets passed on to computations such as the medial axis or the location of maximal inscribed spheres.

For the glass spheres and the sand, an argument can be made that the GB1 networks are physically reasonable because the pore locations are derived from a Delaunay tessellation of the grain locations, which is an accepted method for discretizing the pore space in granular materials (Mellor 1989; Vrettos et al. 1989; Bryant et al. 1993; Thompson and Fogler 1997). These networks contain 4.96 and 6.50 pores/particle for the sphere pack and sand pack, respectively. (These values are lower than the strict Delaunay pore densities because of the merging process.) Pore densities for the VB1 network, which relies on the burn maxima to locate pores, are 15–30% lower than GB1 network (the voxel-based medial axis should produce similar numbers as VB1). However, pore densities are order 10× and 100× higher for the VB2 and VB3 networks, respectively, because they employ direct searches of the void voxels to identify maximal inscribed spheres. For the sand (which has irregular grains), it is likely that some of these additional pores are true maximal inscribed spheres (constrained by the grain structure); however, a significant fraction may be constrained numerically because of the approximate distance function computations that must be made using voxel data.

The trends for the cylinder packing are similar: the VB1 network gives the lowest pore density and the range spans approximately two orders of magnitude. The GB1 data are shown for completeness. However, because this algorithm is designed for use with granular materials, the data cannot be used as a baseline for comparison as it was with the spheres and sand.

Finally, we note that the network porosity is correct for all materials (and is independent of pore density) because the volume assigned to each pore is computed independently of the size of its associated maximal inscribed sphere. For some pore/network combinations, the volume of a pore will be larger than the volume of the maximal sphere. For other pore/network combinations the reverse is true.

4.1.2 Pore Radius

Pore radius is calculated using the maximal inscribed spheres that are associated with each pore. The pore-size distribution for the sphere pack is shown in Fig. 4 for each of the networks. Average pore sizes are reported for all materials and all networks in Table 2. As expected from visualization of the networks, the GB1 and VB1 networks give very similar pore-size distributions for the granular materials. The distribution in the very high density network is shifted toward smaller pores, which is consistent with the ability to find smaller maximal inscribed spheres from a complete voxel search (as opposed to burn maxima or the Delaunay tessellation, both of which will identify the largest pore spaces). The most interesting differences are for the VB2 network, which show markedly different pore-size distributions and average pore sizes. The reason for the difference is that the VB2 network is created from a direct voxel search for maximal inscribed spheres. But, once a sphere has been found, no voxels that lie inside that sphere are used for additional searches. The result is that the dramatic increases in pore density ($\sim 10\times$ in moving from the VB1 to the VB2 networks) were created mostly by the addition of small pores, which were found by exploring the void voxels in the tighter void spaces. This effect shifts the number-average pore size downward (Table 2) and the pore-size distribution to the left (Fig. 4).

These differences are evident in visualizations of the network structures. Comparing the VB1 and the VB2 networks in Fig. 2, notice that the networks share many of the same large "anchor" pores. In the lower-density network, these anchor pores are connected via single pore–throats. In the higher-density VB2 network, these anchor pores are connected via strings of small pores. (In further contrast, the very high density networks contain large numbers of both small and large pores, so the entire void space is filled with caterpillar-like strings of spheres.) While the VB2 and GB1 networks have significantly different pore-size distributions and network structures, it is not possible to declare one more correct than another, at least in the absence of a strict definition for a pore. In fact, it is likely that one network may be more appropriate for some applications and another network more appropriate for others.

4.1.3 Throat Radius

Throat radius is calculated as the radius of the maximal inscribed sphere whose center lies on the surface separating two pores. (Pore–throats have no volume in our network scheme;

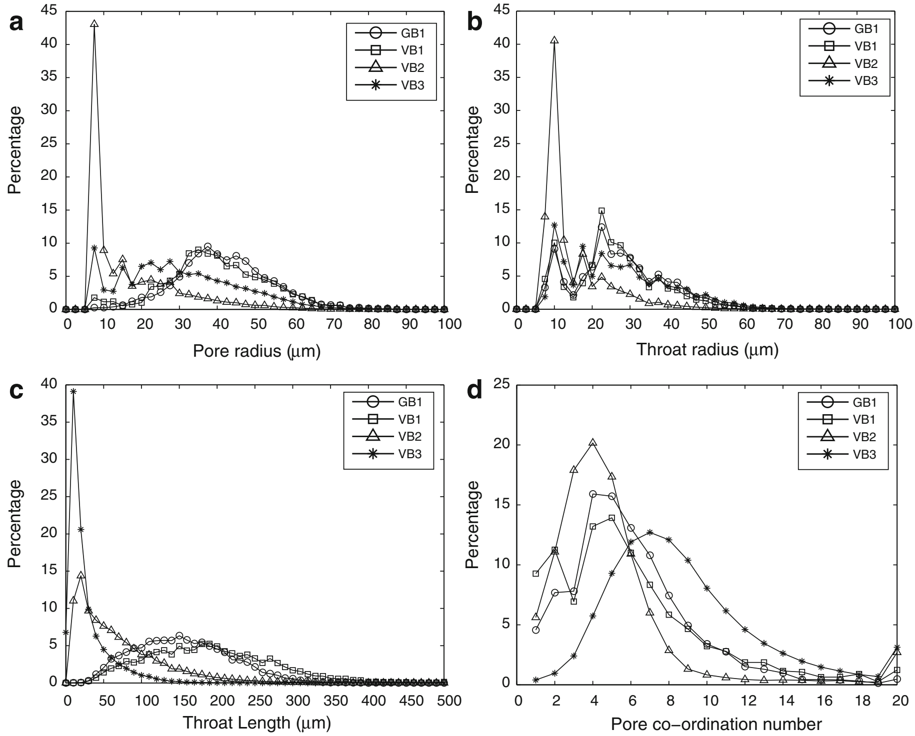

Fig. 4 Comparison of structural properties of pore networks generated from the sphere-pack data: **a** pore size, **b** pore–throat size, **c** pore–throat length, and **d** pore coordination number

therefore, the volumes assigned to any two neighboring pores meet at a surface that in principle should be at the tightest constriction in the connecting passage.) For granular materials, the throat size distributions for three of the four networks are essentially same (Fig. 4), despite the orders of magnitude difference in the number of throats. The one network structure with a different distribution is the VB2 network. For the fibrous material, the throat size distributions are not as consistent across networks as evidenced by the values in Table 2, which shows that the high density network has a larger average throat size. This effect is attributed to the large fraction of overlap between maximal inscribed spheres in the more wide open pore space in the cylinder packing.

4.1.4 Pore Coordination Number

The pore coordination number is the number of pores that are directly connected to a given pore. Determining the pore coordination number from voxelized images can be challenging because the pore boundaries are represented by the Cartesian voxel system, which does not allow for simple surfaces between pore boundaries. This problem is further complicated by a dependence on the voxel resolution, by the range of pore geometries found in natural porous media, and by the network bonds not being aligned with the Cartesian voxel geometry.

The distributions of pore coordination numbers are shown in Fig. 4. The mean values for three of the networks are similar to the mean value determined for granular materials using other techniques (Yanuka et al. 1986; Jerauld and Salter 1990; Al-Raoush et al. 2003). The high-density network exhibits larger values due to the overlap between pores. The tails of the distributions contain coordination numbers that are larger than one might expect from a geometric standpoint. This is caused partly by large pores (which naturally can link to a larger number of small neighbors). It is also a consequence of voxel-based network generation algorithms; similar results have been reported anecdotally for network-generation algorithms from other research groups.

4.2 Single-Phase Flow

Permeability is a spatially averaged parameter that quantifies the macroscopic hydraulic conductance of a porous medium, and is the most basic parameter associated with flow. Consequently, permeability prediction is one of the primary objectives of predictive image-based modeling. In network modeling, the permeability is governed by the hydraulic conductance values assigned to each pore–throat, along with the way in which these pore–throats are interconnected. Hence, it is difficult to imagine that varying the pore or pore–throat density by two orders of magnitude would not have some adverse effect on permeability prediction.

While the goal of this study is not to validate network permeability predictions (but rather to understand the sensitivity of permeability to network structure), we nonetheless present comparative permeabilities obtained from simple empirical equations for completeness (see Table 3).

Simulations are performed for low-Reynolds-number single-phase flow. Constant-pressure boundary conditions are applied on opposing faces of the network and no flow boundary conditions are applied on the remaining faces. The flow rate $q_{i,j}$ between pore i and j is described using Eq. 1. The term $g_{i,j}$ is the hydraulic conductance between pore i and j. Imposing mass conservation for each pore using Eq. 2 creates a system of algebraic equations that can be solved for pressure in each pore. The pressure field is used to solve for flow between individual pores, as well as total flowrate through the network for the applied pressure gradient. This allows permeability to be predicted using the one-dimensional form of Darcy's law (Eq. 3).

$$q_{i,j} = \frac{g_{i,j}}{\mu}\left(P_j - P_i\right) \tag{1}$$

$$\sum_{j=1}^{N} \frac{g_{i,j}}{\mu}\left(P_j - P_i\right) = 0 \tag{2}$$

$$K = \frac{Q}{A}\frac{\mu}{(\Delta P/L)} \tag{3}$$

This procedure was repeated with pressure applied to the other two pairs of opposing faces, thus giving permeabilities along the principal coordinate axes. No significant variations in these directional permeabilities were observed for the granular materials (spheres and sand). For the cylinder packing, permeability is anisotropic. It is dominant in the x-direction, somewhat reduced in y (7–21% smaller values depending on the network), and significantly reduced in z (35–54% smaller values). This suggests a horizontal alignment of fibers.

In order to use Eq. 1, hydraulic conductances must be assigned to each pore–throat in the network. In the past, networks were decorated with hydraulic conductances that were selected randomly from mathematical distributions. However, for image-based modeling, the hydraulic conductances are physical quantities associated with a region of the pore space, and therefore must be estimated from local pore geometry. Many equations have been proposed for this task, which use various combinations of pore and pore–throat radii, pore

Table 3 Single phase permeability (mD) calculated using three hydraulic conductivity models in a single-phase flow simulation

mD	Sphere				Sand				Cylinder			
	GB1	VB1	VB2	VB3	GB1	VB1	VB2	VB3	GB1	VB1	VB2	VB3
Ewing and Gupta	4.34E+04	4.71E+04	4.73E+04	6.57E+04	2.54E+04	2.65E+04	2.56E+04	3.41E+04	3.54E+05	3.82E+05	4.68E+05	8.03E+05
Bryant and Blunt	1.71E+04	1.67E+04	1.62E+04	3.34E+04	9.51E+03	9.48E+03	9.08E+03	1.80E+04	1.22E+05	1.49E+05	1.23E+05	2.87E+05
Thompson and Fogler	3.43E+04	3.35E+04	3.06E+04	2.41E+04	1.85E+04	1.86E+04	1.64E+04	1.30E+04	2.39E+05	2.77E+05	2.43E+05	2.14E+05
Blake–Kozeny	3.88E+04	3.84E+04	3.92E+04	3.88E+04	1.31E+04	1.34E+04	1.32E+04	1.34E+04	2.21E+05	2.21E+05	2.21E+05	2.21E+05
Jackson and James Perm	9.73E+05	9.68E+05	9.78E+05	9.73E+05	4.42E+05	4.45E+05	4.43E+05	4.45E+05	2.03E+06	2.03E+06	2.03E+06	2.03E+06

Permeability values calculated using empirical equations are reported for the sake of comparison or pore–throat surface areas, throat cross-sectional areas, throat lengths, shape factors, etc. We have selected three different equations to use in this study: a single-parameter model (Eq. 4, Ewing and Gupta 1993), two-parameter model (Eq. 5, Bryant and Blunt 1992), and three-parameter model (Eq. 6, Thompson and Fogler 1997). The Ewing–Gupta equation is a function of pore radii only. The Byrant–Blunt equation is a function of both pore–throat radius and length. The Thompson–Fogler equation is a function of pore–throat radius, length and pore to pore–throat aspect ratio. All these parameters represent geometric measurements that are made directly on the voxel image once the pore locations are found (details about the parameters themselves are provided in the references shown).

$$\text{Model:}\quad g_{i,j} = \frac{r_t^3}{3} \tag{4}$$

$$\text{Model:}\quad g_{i,j} = \frac{\pi r_e^4}{8 l_{\mathrm{ptp}}} \tag{5}$$

$$\text{Model:}\quad g_{i,j} = \frac{\pi R_{\mathrm{eff}}^4}{8l}\left[\frac{4l(1+2\zeta_0)(1-\zeta_0)^2}{3R_{\mathrm{eff}}\sin^3(\eta_0)\left(\frac{\lambda_R}{\lambda_R^2+1}+\tan^{-1}(\lambda_R)\right)}\right] \tag{6}$$

4.3 Permeability Results

Figure 5 shows permeabilities for all three porous materials. For each material, permeabilities for the four different networks combined with the three equations for estimating hydraulic conductances are reported. The permeability results lead to a number of important observations:

1. Although the number of pores (and pore–throats) in the networks varies over two orders of magnitude for any one material, permeability variation is much smaller: at worst approximately a factor of two; in most cases significantly less. If we remove the highest-pore-density networks from the results, then we see nearly constant permeability values even as the number of pores changes by a factor of 10–20. This result is encouraging, especially in the absence of a definitive technique for pore discretization. It means that the image-based modeling algorithms are doing their job in the sense that variations in network structure are balanced by the pore-geometry-based schemes used for flow modeling. Reasons for this behavior are discussed below.
2. The highest-pore-density network gives higher permeability estimates when the one- and two-parameter conductance models are used. However, by including the pore–throat aspect ratio (which accounts for the converging–diverging geometry of the throats), this trend is reversed and the highest-pore-density networks exhibit lower permeability than the other three networks (at least for this particular set of conductance formulas).
3. The Ewing–Gupta and Thompson–Fogler equations show different trends when moving from the lower porosity granular materials to the higher-porosity cylinder pack. However, the Bryant–Blunt equation gives very consistent behavior for the three different pore morphologies: essentially constant permeabilities for three of the four networks, but higher permeability for the highest-pore-density network.

4.4 Network Factors Affecting Permeability Computations

The insensitivity of permeability to pore density has been observed previously (Thompson et al. 2008), and was attributed to an effect where the increased number of pore–throats is

Fig. 5 Comparison of scalar permeability calculated using single-phase flow simulations on the networks generated from **a** spheres, **b** sand, and **c** cylinders

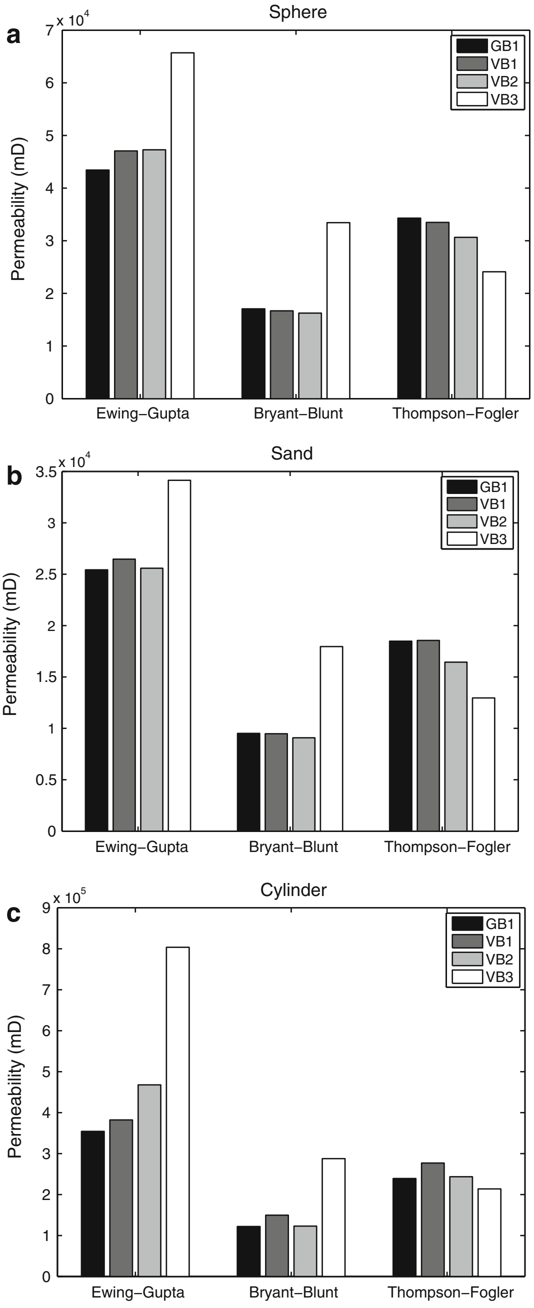

balanced by higher hydraulic conductivities for those throats. Specifically, as the number of pores and pore–throats increases, this corresponds to a larger number of series resistances for flow (which would suggest a lower permeability). But, the higher pore density likewise corresponds to shorter pore–throats, which decreases the resistance of each throat,

Table 4 Comparison of number of pores and throats on the inlet and outlet boundaries of four networks generated using sphere pack image

	GB1		VB1		VB2		VB3	
	Inlet	Outlet	Inlet	Outlet	Inlet	Outlet	Inlet	Outlet
Pore								
X	192	182	161	143	735	864	2969	2920
Y	209	183	168	137	801	774	2925	3165
Z	131	146	104	119	558	584	2071	2458
Throat								
X	876	857	739	869	5208	4254	22600	23988
Y	858	983	742	940	4478	4818	24178	23061
Z	636	674	576	594	3433	3190	20220	16777

thus counteracting the first effect. Current results show that this explanation alone is insufficient: networks that use the one-parameter conductance model exhibit similar insensitivity to pore density despite the fact that they do not exhibit any throat-length dependence. (In fact, the trend is opposite what would be expected from this argument because they give higher permeabilities as the number of resistances in the network increases.) Further analysis suggests that some combination of the following six factors contributes to the permeability in an image-based network model.

Pore density. A larger pore density leads to a larger number of pore–throats, which in turn creates a larger number of series resistances that are encountered during flow across the length of the network. In the absence of other factors, this effect would decrease the computed permeability.

Pore–throat length. A larger pore density would generally lead to shorter pore-to-pore distances. Assuming the hydraulic conductance equation accounts for the pore–throat length (e.g., the Bryant–Blunt and Thompson–Fogler models shown above), then individual pore–throat conductances should increase with pore density.

Inlet/outlet pore density. An increase in the overall pore density will also lead to an increased pore density on the inlet/outlet faces of the domain (see Table 4) as well as an increased density on interior cross sections of the network. To illustrate this effect on fluid conductivity, consider a 2D square lattice with bonds of uniform length and conductance. Assume flow in the x-direction, entering at $x = 0$ and exiting at $x = 1$. Now consider doubling the *linear* density of nodes along the x-direction, which will double the number of resistors in series between $x = 0$ and $x = 1$. A single-parameter conductance model that depends only on bond diameter would cause the overall resistance to double. However, to retain the isotropic structure of the square lattice, one would also need to double the y-direction nodal density. This change would provide twice the number of inlet-to-outlet flow paths along the x-direction, which would exactly offset the increased number of series resistances in the permeability calculation (because each x-direction path would carry half the volumetric flow compared to the original, less-dense lattice).

It would appear that this effect allows the single-parameter conductance model to remain relatively insensitive to pore density. On a 3D cubic lattice, doubling the linear nodal density while keeping the isotropic structure would create four times the number of flow paths from one face to the opposing face. For the 3D image-based networks, we can use the number of inlet/outlet pores as a surrogate measure of this effect. Comparing the VB1 and the VB2 networks from the sphere pack (because they have essentially the same permeabilities based on the one-parameter Ewing–Gupta model), the network statistics suggest a change in linear pore density of approximately $(35403/2363)^{1/3} = 2.47$. The expected increase in inlet or outlet throats would therefore be factor of $(2.47)^2 = 6.08$. Comparing these two networks, the actual increase is 5.69, suggesting that this effect may contribute substantially in maintaining consistent permeabilities for different networks.

Pore coordination number. The argument given above relies on the assumption that as the pore density increases, pores remain connected to one another in a manner similar to the lower-density networks. In the networks generated from real images, the average pore coordination number remains relatively constant (for any given material) for the GB1, VB1, and VB2 networks, suggesting that this assumption is reasonable. However, pore coordination number increases significantly for the highest-density VB3 networks relative to the other three.

Pore connectivity. In addition to the average coordination number (above) the spatial connectivity is important because the total macroscopic flow associated with the material permeability can be dominated by a relatively small fraction of the pore space that provides the most conductivity pathways for flow. The transition from the GB1 network (or the VB1 network) to the VB2 network involves the addition of a very large number of pores (approximately 10 times as many), most of which are small pores that fill in between the large pores in the low-density networks: see Figs. 2 and 4. If these additional pores interrupt the connectivity of the dominant flow channels, it would impact the permeability. In contrast, if the dominant flow channels remain connected as the pore density increases, the addition of the small pores should have little consequence.

Conductance equation. The various throat conductance models available in literature include different combinations of pore–throat geometry as shown by the three conductance formulas chosen for this study. Hence, the choice of conductance formula can impact the relationship between pore parameters and permeability.

The results and discussion in this section should highlight a few important points:

1. Because the relationship between network structure and permeability depends on a number of related factors, it is difficult to anticipate a priori how a change in network structure will affect fluid flow.
2. It is reasonable to assume that networks having dramatically different structures can generate consistent permeability predictions if they are properly designed.
3. The use of fundamental, geometric-based computations to assign network properties may be an effective way to help ensure that flow computations are independent of the specific network generation algorithm that is chosen.

4.5 Quasi-Static Drainage

Generally, multiphase flow is more sensitive to pore structure than single-phase flow because of the large impact of pore structure on the dynamics and location of fluid–fluid interfaces. To help assess the impact that network structure has on interfacial phenomena (i.e., different networks for the same porous material), quasi-static displacements were performed on the set of models. These simulations model immiscible displacement starting at a saturation $S_\mathrm{w} = 1$ (pore space saturated with wetting phase) to a final point where a large fraction of the pore space has been invaded by the non-wetting phase. Quasi-static simulations neglect fluid viscosity, which in turn means that the model does not depend on time. The physical interpretation of the quasi-static displacement is a capillary-pressure-dominated invasion of the non-wetting phase, which is sufficiently slow so that pressure gradients do not develop in either fluid phase. In our simulations the effect of gravity is neglected, although this restriction can easily be removed.

To generate macroscopic capillary pressure curves using a network model, local pore capillary pressure functions (vs. saturation) are needed for each pore. Unlike the monotonically increasing macroscopic capillary pressure curve (as S_w decreases), the pore-scale capillary pressure function can undergo a minimum, which separates equilibrium and non-equilibrium branches of the curve. At the smallest non-wetting phase saturations, the local capillary pressure can be large if the non-wetting phase has squeezed into the pore through a small pore–throat. This configuration represents a non-equilibrium state: once entry has started, the interface will rapidly invade (a Haines jump), retract (if the local capillary pressure drops), or become disconnected and trapped due to a snap-off event. At some intermediate saturation value, the capillary pressure reaches a minimum, which corresponds to a fluid–fluid configuration with the minimum allowable curvature (constrained by local geometry and contact angles). Then, to further increase the non-wetting-phase saturation requires larger capillary pressures that squeeze interfaces into corners of the pores. The branch of the curve between the minimum capillary pressure and $S_\mathrm{w} \rightarrow 0$ is an equilibrium branch.

Capturing this pore-scale behavior in a local capillary pressure function is difficult because of the strong dependence on pore geometry, invasion sequence, and surface properties (e.g., contact angle), and also because part of the curve reflects the fast, non-equilibrium behavior associated with the Haines jumps. For simplicity, most networks of immiscible displacement ignore the fast dynamics, and capture only equilibrium behavior. In our simulations we also neglect snap-off behavior, and we use the capillary pressure function for a cubic pore to provide the basic functionality for the pore capillary pressure function as described by Thompson (2002).

To perform the quasi-static drainage simulation, a positive capillary pressure is applied on one face of the network. A search is performed to find any pore–throats on the inlet face that are accessible at this capillary pressure, and invasion is allowed into the connecting pores. Invasion continues as long as newly accessible throats can be invaded at the current capillary pressure. Once an equilibrium point is reached, the applied capillary pressure at the inlet is increased and the process continues.

The capillary pressure curves generated from quasi-static drainage simulations are shown in Fig. 6. For all three porous materials, the GB1 and VB1 curves overlap, suggesting that the pore and pore–throat size distributions (along with how the pores are connected) are similar for both the grain-based approach and the fast voxel-based approach. As the pore density increases, the elbow in the capillary pressure curve becomes less sharp. This is not unexpected: a larger number of pores and connections should provide for a smoother transition across the saturation range. Figure 7 helps illustrate the effect; it shows a 2D saturation map averaged over the thickness of the networks at four different saturations for the different networks structures of the sphere packing. The low-density networks show larger and more distinct pockets of wetting phase as the displacement progresses. Whereas, the fluid phases are distributed more evenly in the high density networks. This suggests that at a given saturation (e.g., $S_\mathrm{w} = 0.4$), the higher density networks were able to provide for a fluid configuration in which the non-wetting phase did not yet have to access the smallest pores, which in turn corresponds to the less-sharp elbow: S_w reaches a value of 0.4 at a lower capillary pressure.

Capillary pressure curves are commonly used to compute pore-size distributions, and we have constructed capillary pressure curves from Fig. 7 data using the van-Genuchten model (van Genuchten 1980; Van Genuchten et al. 1991). The pore-size distributions generated in this manner are much more consistent with one another than those shown in Fig. 4

Fig. 6 Capillary pressure versus saturation relation calculated using quasi-static drainage simulation: **a** spheres, **b** sand, and **c** cylinders

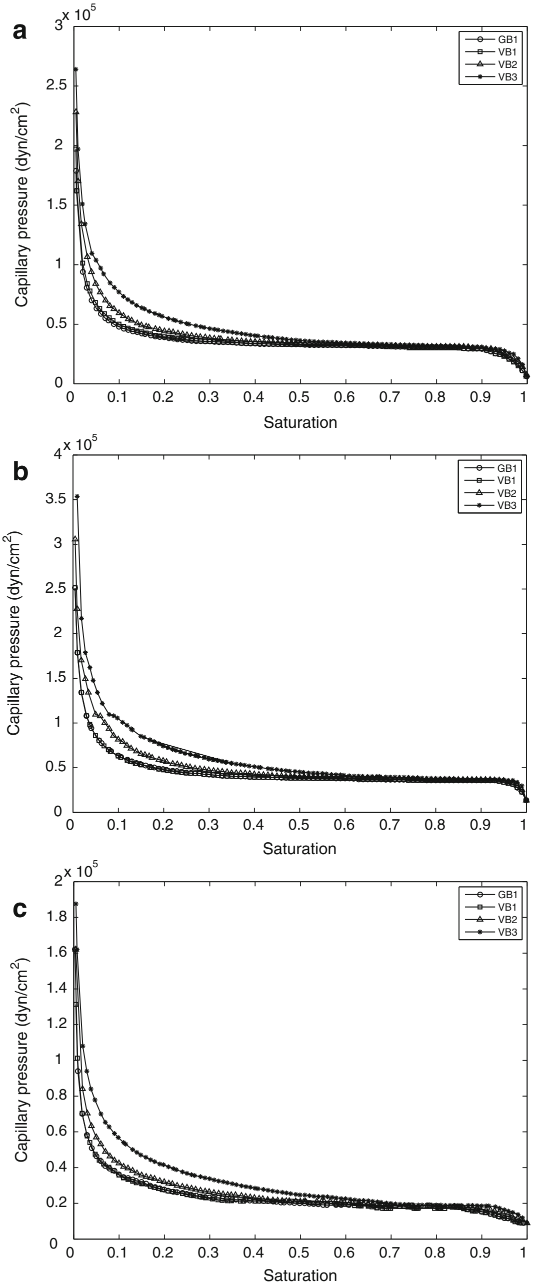

(the lower-density networks have slightly sharper peaks, which are also shifted to slightly larger pore size). While this result again suggests that the different network structures can reproduce similar physics, a direct comparison of the two pore-size distributions is not possible since the network data produce a number-based distribution of pore sizes, whereas the capillary-pressure-based result is volume-based.

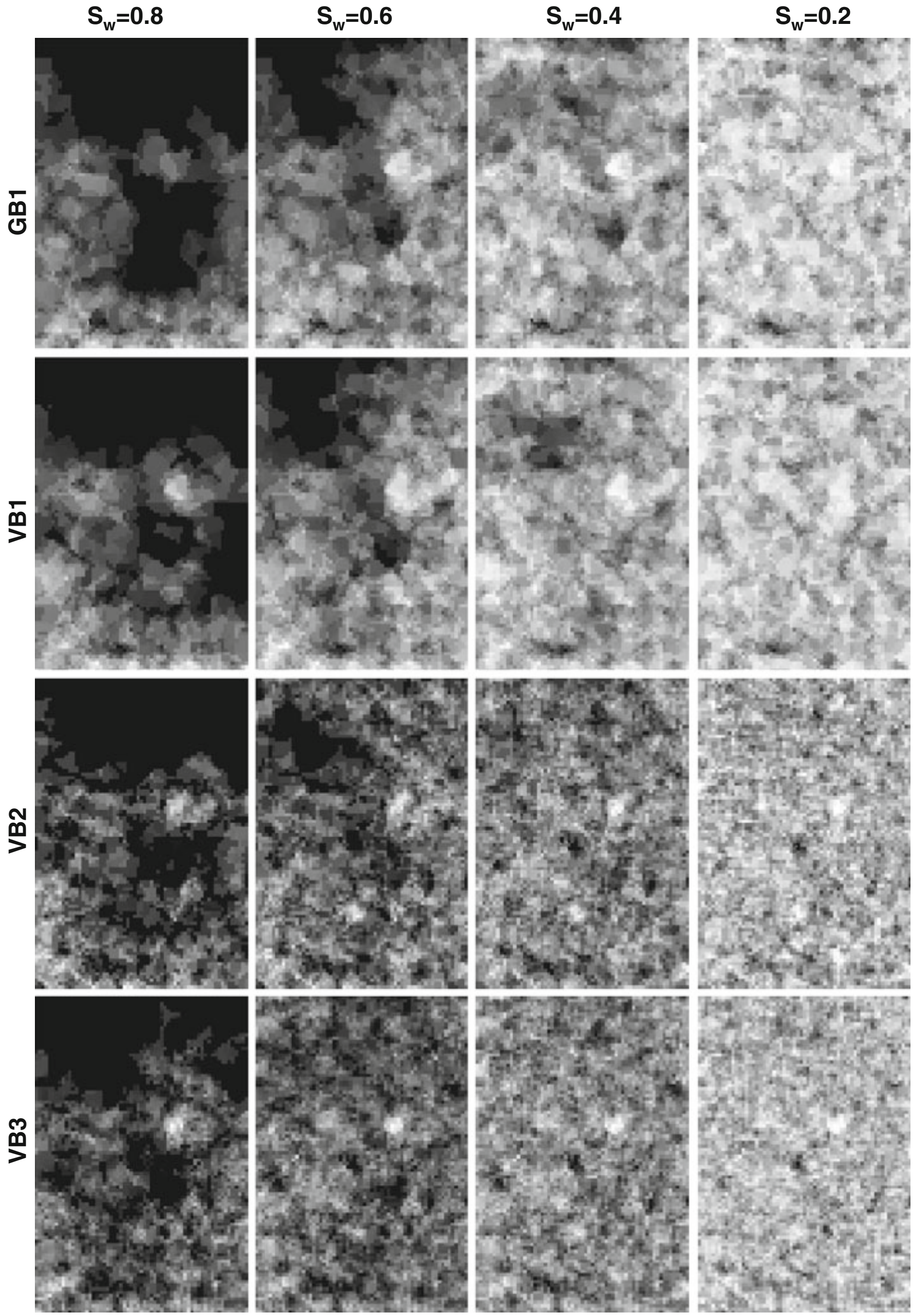

Fig. 7 Saturation map showing distribution of water (*black*) and hexadecane (*white*) in the networks generated from the sphere-pack data. The saturation is averaged over the thickness of the network

5 Conclusion

Image-based network modeling is becoming a widely applied tool for understanding pore-scale behavior in porous media. A number of network-generation strategies have been proposed, but it is not yet clear how critical the network generation process is to the success of the subsequent network modeling procedure. We have used XCT images of three different porous media to begin understanding the impact of differences in network structure on modeling. For each porous medium, four different networks were created, which exhibit dramatically different network properties (in particular, the number of pores, which is reported as pore density). Analysis of network structure, simulation of single-phase permeability, and simulation of quasi-static drainage were used to interpret the impact of the network structure on simulation results.

We argue that with the exception of the simplest types of materials (e.g., structured sphere packings), no single network model is uniquely correct; in continuum pore spaces composed of converging–diverging and interconnected channels it is difficult to prescribe definitions for pores and pore–throats precisely. This problem is further exacerbated by the necessary use of voxelized data to describe the original pore structure, which contain both experimental error and limitations in resolution. These errors/uncertainties prevent the precise computation of parameters such as distance functions (i.e., void locations to surfaces), pore diameters, or the location of a maximal inscribed spheres.

In the networks we use here, the large variations in pore density are a result of two factors: different methods for seeding the search for pores (i.e., defined as maximal inscribed spheres), and different settings in the merge criteria (that merges overlapping inscribed spheres to created single pores). Generally, the fast algorithms create low-density networks with little or no overlap in inscribed pores, and therefore also generate longer pore–throats. More complete pore searches are slow, resulting in higher pore densities and shorter pore–throats. In the highest-density case, the pore networks are caterpillar-like structures of overlapping pores that snake through the pore space. In all cases, the pore and pore–throat parameters are measured directly from the surrounding material. Hence, porosity, total pore volume, and surface area are conserved (and correct) relative to the original voxel image. The pore density affects secondary parameters, such as pore-size distribution and pore interconnectivity. However, the relationship is not always proportional or obvious. For instance, the lowest- and highest-density network shown here have similar pore-size distributions, while the peak in the pore-size distribution from the middle-density VB2 network is shifted far to the left (for reasons explained in the article).

The most important result shown is the relative insensitivity of predicted single-phase permeability for a given material in spite of orders-of-magnitude changes in pore density, even for the most primitive pore–throat conductance formulas. We view this insensitivity is a beneficial trait (i.e., since the original sample has only one correct permeability) and attribute it to the use of physically representative network modeling, which when applied correctly precludes the use of adjustable parameters for modeling and maps dimensional geometric quantities onto the network structure.

Capillary pressure curves for quasi-static drainage are moderately sensitive to network structure. This result is expected given the sensitivity of interfacial phenomena to pore structure, some of which is captured in the network modeling algorithms. Generally, the low-pore-density capillary pressure curves have a sharper shoulder at the transition from the plateau capillary pressure to the steep rise. This is caused by fewer options for the invasion pattern when simulating the injection of non-wetting phase. When pore-size distributions are

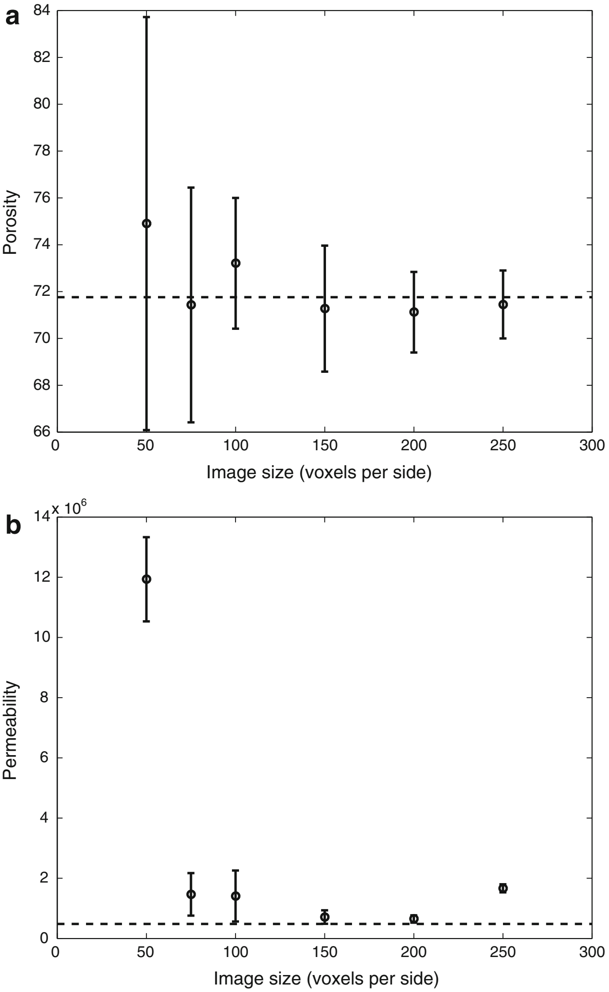

Fig. 8 Test for REV for cylinder image. The *dashed line* indicates properties of 350 × 350 × 520 image: **a** porosity and **b** permeability. *Error bars* show variation of five randomly sampled locations from the same image

generated from the capillary pressure curves, the results of these differences include narrower peaks at larger pore sizes for the lower-density networks.

We expect that the correctness or quality of one network versus another (for the same porous material) will depend on the application for which it is used. For example, the VB2 networks shown in this article, which contain sharp peaks at very small pore sizes, are not the best choice for characterization. However, it is not difficult to believe that this same structure might prove effective as a pore-space discretization for modeling transport because the network better conforms to the tight regions of the pore space.

Acknowledgments Funding for this study was provided by the PoreSim Research Consortium: members included BP America, Millipore and Schlumberger during the time of this work. Preliminary XCT work was performed at the tomography beamline in the Center for Advanced Mechanical Devices, Louisiana

State University. XCT work was performed at GeoSoilEnviroCARS (Sector 13), Advanced Photon Source (APS), Argonne National Laboratory. GeoSoilEnviroCARS is supported by the National Science Foundation-Earth Sciences (EAR-0622171) and Department of Energy-Geosciences (DE-FG02-94ER14466). Use of the Advanced Photon Source was supported by the U. S. Department of Energy, Office of Science, Office of Basic Energy Sciences, under Contract No. DE-AC02-06CH11357. We also would like to thank Qiang Sheng, Department of Chemical Engineering, Louisiana State University, for the help with hydraulic conductivity calculations.

Appendix

The data for the cylinder packing (350 × 350 × 520 voxels) has approximately 72% porosity and thus contains more than 45 million void voxels. For the VB3 network algorithm, each void voxel is searched as a potential seed, which requires a non-linear optimization to calculate the inscribed sphere radius. This makes the process computationally expensive. To be able to calculate pore structure properties and to compare between all four networks, a smaller image of size 150 × 150 × 150 was chosen in this study. To confirm that the smaller size image contains a representative elementary volume (REV) for porosity and permeability, we randomly sampled various sized images from the large image, and created networks using the VB1 algorithm. Figure 8 shows a comparison of porosity and single-phase permeability of various small images with the original large image, suggesting that the image size 150 × 150 × 150 is sufficiently large for the analyses performed here.

References

Adler, P.M., Jacquin, C.G., Quiblier, J.A.: Flow in simulated porous media. Int. J. Multiphase Flow **16**(4), 691–712 (1990)

Al-Kharusi, A.S., Blunt, M.J.: Network extraction from sandstone and carbonate pore space images. J. Pet. Sci. Eng. **56**(4), 219–231 (2007)

Al-Kharusi, A.S., Blunt, M.J.: Multiphase flow predictions from carbonate pore space images using extracted network models. Water Resour. Res. **44**, W06S01, (2008). doi:10.1029/2006WR005695. http://www.agu.org/pubs/crossref/2008/2006WR005695.shtml

Al-Raoush, R., Thompson, K., Willson, C.S.: Comparison of network generation techniques for unconsolidated porous media. Soil Sci. Soc. Am. J. **67**(6), 1687–1700 (2003)

Al-Raoush, R.I., Willson, C.S.: Extraction of physically realistic pore network properties from three-dimensional synchrotron X-ray microtomography images of unconsolidated porous media systems. J. Hydrol. **300**(1–4), 44–64 (2005a)

Al-Raoush, R.I., Willson, C.S.: A pore-scale investigation of a multiphase porous media system. J. Contam. Hydrol. **77**(1–2), 67–89 (2005b)

Arns, C.H., Knackstedt, M.A., Pinczewski, W.V., Martys, N.S.: Virtual permeametry on microtomographic images. J. Pet. Sci. Eng. **45**(1–2), 41–46 (2004)

Auzerais, F.M., Dunsmuir, J., Ferreol, B.B., Martys, N., Olson, J., Ramakrishnan, T.S., Rothman, D.H., Schwartz, L.M.: Transport in sandstone: a study based on three dimensional microtomography. Geophys. Res. Lett. **23**(7), 705–708 (1996)

Baldwin, C.A., Sederman, A.J., Mantle, M.D., Alexander, P., Gladden, L.F.: Determination and characterization of the structure of a pore space from 3D volume images. J. Colloid Interface Sci. **181**(1), 79–92 (1996)

Balhoff, M.T., Thompson, K.E.: Modeling the steady flow of yield-stress fluids in packed beds. Aiche J. **50**(12), 3034–3048 (2004)

Balhoff, M.T., Thompson, K.E., Hjortso, M.: Coupling pore-scale networks to continuum-scale models of porous media. Comput. Geosci. **33**(3), 393–410 (2007)

Balhoff, M., Thomas, S., Wheeler, M.: Mortar coupling and upscaling of pore-scale models. Comput. Geosci. **12**(1), 15–27 (2008)

Bekri, S., Xu, K., Yousefian, F., Adler, P.M., Thovert, J.F., Muller, J., Iden, K., Psyllos, A., Stubos, A.K., Ioannidis, M.A.: Pore geometry and transport properties in North Sea chalk. J. Pet. Sci. Eng. **25**(3–4), 107–134 (2000)

Bhattad, P., Willson, C.S., Thompson, K.E.: Segmentation of low-contrast three-phase X-ray tomography images of porous media. In: Alshibli, K.A., Reed, A.H. (eds.) Advances in Computed Tomography for Geomaterials, pp. 254–261. ISTE, London; Willey, Hoboken, NJ, USA (2010)

Blunt, M., King, M.J., Scher, H.: Simulation and theory of 2-phase flow in porous-media. Phys. Rev. A **46**(12), 7680–7699 (1992)

Blunt, M.J., Fenwick, D.H., Zhou, D.: What determines residual oil saturation in three-phase flow? Proceedings—SPE/DOE Symposium on Improved Oil Recovery, 9th, Tulsa, OK, vol. 2, pp 371–380, April 17–20, 1994

Botto, R.E., Cody, G.D., Dieckman, S.L., French, D.C., Gopalsami, N., Rizo, P.: Three-dimensional magnetic resonance microscopy of materials. Solid State Nucl. Magn. Reson. **6**(4), 389–402 (1996)

Bryant, S., Blunt, M.: Prediction of relative permeability in simple porous media. Phys. Rev. A **46**(4), 2004–2011 (1992)

Bryant, S., Johnson, A.: Wetting phase connectivity and irreducible saturation in simple granular media. J. Colloid Interface Sci. **263**(2), 572–579 (2003)

Bryant, S., Mellor, D., Cade, C.: Physically representative network models of transport in porous media. Aiche J. **39**(3), 387–396 (1993)

Chatzis, I., Dullien, F.A.L.: Modeling pore structure by 2-D and 3-D networks with application to sandstones. J. Can. Pet. Technol. **16**(1), 97–108 (1977)

Dalla, E., Hilpert, M., Miller, C.T.: Computation of the interfacial area for two-fluid porous medium systems. J. Contam. Hydrol. **56**(1–2), 25–48 (2002)

Delerue, J.F., Perrier, E., Yu, Z.Y., Velde, B.: New algorithms in 3D image analysis and their application to the measurement of a spatialized pore size distribution in soils. Phys. Chem. Earth A: Solid Earth Geodesy **24**(7), 639–644 (1999)

Ewing, R.P., Gupta, S.C.: Percolation and permeability in partially saturated networks. Water Resour. Res. **29**(9), 3179–3188 (1993)

Fatt, I.: The network model of porous media 1. Capillary pressure characteristics. Trans. Am. Inst. Min. Metall. Eng. **207**(7), 144–159 (1956)

Fenwick, D.H., Blunt, M.J.: Three-dimensional modeling of three phase imbibition and drainage. Adv. Water Resour. **21**(2), 121–143 (1998)

Frangakis, A.S., Hegerl, R.: Noise reduction in electron tomographic reconstructions using nonlinear anisotropic diffusion. J. Struct. Biol. **135**(3), 239–250 (2001)

Gaviglio, P., Bekri, S., Vandycke, S., Adler, P.M., Schroeder, C., Bergerat, F., Darquennes, A., Coulon, M.: Faulting and deformation in chalk. J. Struct. Geol. **31**(2), 194–207 (2009)

Gladkikh, M., Bryant, S.: Prediction of interfacial areas during imbibition in simple porous media. Adv. Water Resour. **26**(6), 609–622 (2003)

Gladkikh, M., Bryant, S.: Prediction of imbibition in unconsolidated granular materials. J. Colloid Interface Sci. **288**(2), 526–539 (2005)

Gladkikh, M., Bryant, S.: Prediction of imbibition from grain-scale interface movement. Adv. Water Resour. **30**(2), 249–260 (2007)

Hilpert, M., McBride, J.F., Miller, C.T.: Investigation of the residual-funicular nonwetting-phase-saturation relation. Adv. Water Resour. **24**(2), 157–177 (2000)

Hilpert, M., Glantz, R., Miller, C.T.: Calibration of a pore-network model by a pore-morphological analysis. Transp. Porous Media **51**(3), 267–285 (2003)

Jackson, G.W., James, D.F.: The permeability of fibrous porous media. Can. J. Chem. Eng. **64**(3), 364–374 (1986)

Jerauld, G.R., Salter, S.J.: The effect of pore-structure on hysteresis in relative permeability and capillary pressure: Pore-level modeling. Transp. Porous Media **5**(2), 103–151 (1990)

Jiang, Z., Wu, K., Couples, G., Van Dijke, M.I.J., Sorbie, K.S., Ma, J.: Efficient extraction of networks from three-dimensional porous media. Water Resour. Res. **43**(12), 17 (2007)

Kose, K.: 3D NMR imaging of foam structures. J. Magn. Reson. A **118**(2), 195–201 (1996)

Lindquist, W.B., Lee, S.M., Coker, D.A., Jones, K.W., Spanne, P.: Medial axis analysis of void structure in three-dimensional tomographic images of porous media. J. Geophys. Res. Solid Earth **101**(B4), 8297–8310 (1996)

Lindquist, W.B., Venkatarangan, A.: Investigating 3D geometry of porous media from high resolution images. Phys. Chem. Earth A: Solid Earth Geodesy **24**(7), 593–599 (1999)

Lymberopoulos, D.P., Payatakes, A.C.: Derivation of topological, geometrical, and correlational properties of porous media from pore-chart analysis of serial section data. J. Colloid Interface Sci. **150**(1), 61–80 (1992)

Mahmud, W.M.: The effect of fluid saturation profiles on three-phase oil relative permeabilities and oil recovery. In: SPE Annual Technical Conference and Exhibition. Society of Petroleum Engineers, Anaheim, CA, USA (2007)

Mellor, D.W.: Random close packing of equal spheres; structure and implications for use as a model porous medium. PhD thesis, Open University, Milton Keynes, UK (1989)

Mickel, W., Munster, S., Jawerth, L.M., Vader, D.A., Weitz, D.A., Sheppard, A.P., Mecke, K., Fabry, B., Schroder-Turk, G.E.: Robust pore size analysis of filamentous networks from three-dimensional confocal microscopy. Biophys. J. **95**(12), 6072–6080 (2008)

Neethirajan, S., Jayas, D.S.: Analysis of pore network in three-dimensional (3D) grain bulks using X-ray CT images. Transp. Porous Media **73**(3), 319–332 (2008)

Oh, W., Lindquist, W.B.: Image thresholding by indicator kriging. IEEE Trans. Pattern Anal. Mach. Intell. **21**(7), 590–602 (1999)

Oren, P.E., Bakke, S.: Process based reconstruction of sandstones and prediction of transport properties. Transp. Porous Media **46**(2–3), 311–343 (2002)

Pauli, J., Scheying, G., Mugge, C., Zschunke, A., Lorenz, P.: Determination of the pore widths of highly porous materials with NMR microscopy. Fresenius J. Anal. Chem. **357**(5), 508–513 (1997)

Petrovic, A.M., Siebert, J.E., Rieke, P.E.: Soil bulk density analysis in three dimensions by computed tomographic scanning. Soil Sci. Soc. Am. J. **46**(3), 445–450 (1982)

Prodanovic, M., Lindquist, W.B., Seright, R.S.: 3D image-based characterization of fluid displacement in a Berea core. Adv. Water Resour. **30**(2), 214–226 (2007)

Pudney, C.: Distance-based skeletonization of 3D images. In: TENCON '96. Proceedings. 1996 IEEE TENCON. Digital Signal Processing Applications. vol. 201, pp. 209–214 (1996)

Pudney, C.: Distance-ordered homotopic thinning: a skeletonization algorithm for 3D digital images. Comput. Vis. Image Underst. **72**(3), 404–413 (1998)

Ruffino, L., Mann, R., Oldman, R., Stitt, E.H., Boller, E., Cloetens, P., DiMichiel, M., Merino, J.: Using x-ray microtomography for characterisation of catalyst particle pore structure. Can. J. Chem. Eng. **83**(1), 132–139 (2005)

Sahimi, M., Heiba, A.A., Ted Davis, H., Scriven, L.E.: Dispersion in flow through porous media—II. Two-phase flow. Chem. Eng. Sci. **41**(8), 2123–2136 (1986)

Saito, T., Toriwaki, J.: Reverse distance transformation and skeletons based upon the euclidean metric for N-dimensional digital binary pictures. IEICE Trans. Inf. Syst. **E77**(9), 1005–1016 (1994)

Scharr, H., Spies, H.: Accurate optical flow in noisy image sequences using flow adapted anisotropic diffusion. Signal Process. Image Commun. **20**(6), 537–553 (2005)

Silin, D., Patzek, T.: Pore space morphology analysis using maximal inscribed spheres. Physica A **371**(2), 336–360 (2006)

Spanne, P., Thovert, J.F., Jacquin, C.J., Lindquist, W.B., Jones, K.W., Adler, P.M.: Synchrotron computed microtomography of porous media: topology and transports. Phys. Rev. Lett. **73**(14), 2001 (1994)

Thompson, K.E.: Pore-scale modeling of fluid transport in disordered fibrous materials. Aiche J. **48**(7), 1369–1389 (2002)

Thompson, K.E., Fogler, H.S.: Modeling flow in disordered packed beds from pore-scale fluid mechanics. Aiche J. **43**(6), 1377–1389 (1997)

Thompson, K.E., Willson, C.S., Zhang, W.: Quantitative computer reconstruction of particulate materials from microtomography images. Powder Technol. **163**(3), 169–182 (2006)

Thompson, K.E., Willson, C.S., White, C.D., Nyman, S.L., Bhattacharya, J.P., Reed, A.H.: Application of a new grain-based reconstruction algorithm to microtomography images for quantitative characterization and flow modeling. Spe J. **13**(2), 164–176 (2008)

Thovert, J.F., Salles, J., Adler, P.M.: Computerized characterization of the geomety of real porous media: their discretization, analysis and interpretation. J. Microsc. **170**, 65–79 (1993)

van Genuchten, M.T.: A closed-form equation for predicting the hydraulic conductivity of unsaturated soils. Soil Sci. Soc. Am. J. **44**(5), 892–898 (1980)

Van Genuchten, M.T., Leij, F.J., Yates, S.R.: The RETC code for quantifying the hydraulic functions of unsaturated soils. United states environmental protection agency, EPA/600/2-91/065 (1991)

Vogel, H.J.: A numerical experiment on pore size, pore connectivity, water retention, permeability, and solute transport using network models. Eur J Soil Sci **51**(1), 99–105 (2000)

Vogel, H.J., Roth, K.: Quantitative morphology and network representation of soil pore structure. Adv. Water Resour. **24**(3-4), 233–242 (2001)

Vrettos, N.A., Imakoma, H., Okazaki, M.: Transport properties of porous media from the microgeometry of a three-dimensional voronoi network. Chem. Eng. Process. Process Intensif. **26**(3), 237–246 (1989)

Wardlaw, N.C., Li, Y., Forbes, D.: Pore-throat size correlation from capillary-pressure curves. Transp. Porous Media **2**(6), 597–614 (1987)

Weickert, J., Scharr, H.: A scheme for coherence-enhancing diffusion filtering with optimized rotation invariance. J. Visual Commun. Image Represent. **13**(1-2), 103–118 (2002)

Yanuka, M., Dullien, F.A.L., Elrick, D.E.: Percolation processes and porous media: I. Geometrical and topological model of porous media using a three-dimensional joint pore size distribution. J. Colloid Interface Sci. **112**(1), 24–41 (1986)

Zhang, W.: Experimental and computational analysis of random cylinder packings with applications. Ph.D. thesis, Louisiana State University, Baton Rouge, USA (2006)